

Incommensurate magnetism near quantum criticality in CeNiAsO

Shan Wu,^{1,2,*} W. A. Phelan,¹ L. Liu,³ J. R. Morey,¹ J. A. Tutmaher,¹ J. C. Neufeind,⁴ Ashfia Huq,⁵ Matthew B. Stone,⁵ M. Feyngenson,⁶ David W. Tam,⁷ Benjamin A. Frandsen,⁸ Benjamin Trump,⁹ Cheng Wan,¹ S. R. Dunsiger,¹⁰ T. M. McQueen,^{1,11} Y. J. Uemura,³ and C. L. Broholm^{1,11,12}

¹*Department of Physics and Astronomy and Institute for Quantum Matter,
Johns Hopkins University, Baltimore, Maryland 21218, USA*

²*Department of Physics, University of California Berkeley, Berkeley, California 94720, USA*

³*Department of Physics, Columbia University, New York, New York 10027, USA*

⁴*Oak Ridge National Laboratory, Chemical and Engineering Materials Division, Oak Ridge, Tennessee 37831, USA*

⁵*Oak Ridge National Laboratory, Neutron Scattering Division, Oak Ridge, Tennessee 37831, USA*

⁶*Juelich Centre for Neutron Science, Forschungszentrum Juelich GmbH, 52425 Juelich, Germany*

⁷*Department of Physics and Astronomy, Rice University, Houston, Texas 77005, USA*

⁸*Department of Physics and Astronomy, Brigham Young University, Provo, Utah 84602, USA*

⁹*NIST Center for Neutron Research, National Institute of Standards and Technology, Gaithersburg, Maryland 20899, USA*

¹⁰*Department of Physics, Simon Fraser University, Burnaby, B.C., Canada*

¹¹*Department of Materials Science and Engineering,
Johns Hopkins University, Baltimore, Maryland 21218, USA*

¹²*Oak Ridge National Laboratory, Quantum Condensed Matter Division, Oak Ridge, Tennessee 37831, USA*

(Dated: June 18, 2021)

We report the discovery of incommensurate magnetism near quantum criticality in CeNiAsO through neutron scattering and zero field muon spin rotation. For $T < T_{N1} = 8.7(3)$ K, a second order phase transition yields an incommensurate spin density wave with wave vector $\mathbf{k} = (0.44(4), 0, 0)$. For $T < T_{N2} = 7.6(3)$ K, we find co-planar commensurate order with a moment of $0.37(5) \mu_B$, reduced to 30 % of the saturation moment of the $|\pm \frac{1}{2}\rangle$ Kramers doublet ground state, which we establish through inelastic neutron scattering. Muon spin rotation in CeNiAs_{1-x}P_xO shows the commensurate order only exists for $x \leq 0.1$ so we infer the transition at $x_c = 0.4(1)$ is between an incommensurate longitudinal spin density wave and a paramagnetic Fermi liquid.

The competing effects of intra-site Kondo screening and inter-site Ruderman-Kittel-Kasuya-Yosida (RKKY) interactions in rare earth intermetallics epitomize the strongly correlated electron problem. While the Néel and Kondo lattice limits are well understood [1], the transition between them is far from. It involves an increase in the volume enclosed by the Fermi surface (FS) as the $4f$ electron is incorporated on the Kondo lattice side of the transition [2, 3]. Deviations from the $\rho \propto T^2$ dependence of resistivity is interpreted as indicative of the associated quantum criticality, which is denoted as “local” because it involves the entire FS. In support of this concept, compounds with the requisite transport anomalies have been discovered where physical properties that involve averages over distinct regions of momentum space have related critical exponents. The eventual transition to magnetic order when RKKY interactions dominate can coincide with the localization transition or occur within the large or small FS phases. Clearly the nature of the corresponding quantum critical point is strongly affected as magnetic ordering is momentum selective and breaks time reversal symmetry.

Exploration of model systems is essential to uncover the overall phase diagram of this complex strongly correlated regime. CeCu_{6-x}Au_x provided a first example of local criticality. de Haas-van Alphen measurements provide evidence for an abrupt rearrangement of the FS in CeRhIn₅ at 2.25 GPa [4–6]. A step change in

the Hall coefficient of YbRh₂Si₂ coupled with anomalous and yet unexplained critical exponents at the field driven ferromagnetic transition have been interpreted as evidence the magnetic and the electron localization transitions coincide [7–11]. Each compound adds unique insights and distinct experimental opportunities.

Isostructural to the 1111 iron pnictides, CeNiAsO is an exciting new addition to the landscape of strongly correlated electron systems [12]. Magnetically ordered at low- T and ambient pressure, substitution of P for As or pressure drives CeNiAs_{1-x}P_xO to a paramagnetic Fermi-liquid. Non-Fermi-liquid transport is found up to the critical pressure $P_c = 6.5$ kbar and the critical composition $x_c = 0.4(1)$ and a sign change in the Hall coefficient at P_c indicates FS reconstruction [13]. CeNiAsO differs from other systems studied to date in having two magnetic phase transitions [12].

In this letter we determine the corresponding magnetic phases and examine their interplay with FS reconstruction. We show the upper transition is to an incommensurate longitudinal SDW state with wave vector $\mathbf{k} = (0.44(4), 0, 0)$ that closely matches the umklapp wave vector ($2\mathbf{k}_f$) of the small FS. The second transition yields co-planar commensurate order with a low- T ordered moment reduced to 30% of the saturation moment of the nominal $|\pm \frac{1}{2}\rangle$ Kramers doublet ground state. P doping suppresses the commensurate phase but retains the SDW perhaps all the way to the critical

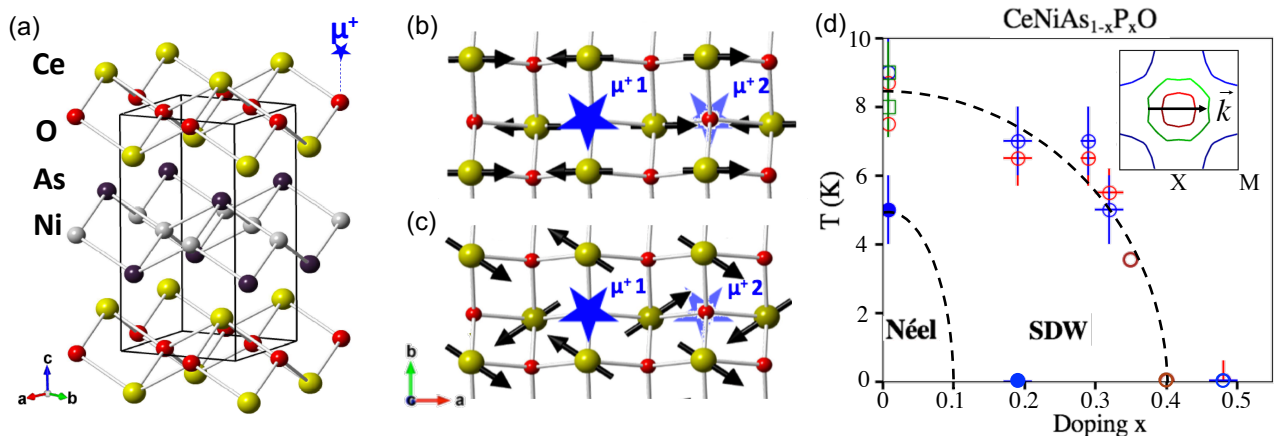


FIG. 1: (a) Crystallographic structure of CeNiAsO, and spin structure for $T_{N2} < T < T_{N1}$ (b) and $T < T_{N2}$ (c). Blue stars indicate the single crystallographic muon site. Two equivalent muon sites above and below oxygen site become inequivalent within the magnetically ordered state. (d) Temperature-doping phase diagram. Red, blue, and green symbols are from specific heat, μ SR, and neutron data respectively. Brown dots are from Luo et al. [13]. We assign open (closed) symbols to the higher (lower) T transition. The inset to (d) shows the $q_z = 0$ small Fermi surface excluding $4f$ electrons. The arrow shows the magnetic wave vector, which connects extended areas of the Fermi surface. The dashed lines are guides to the eye.

concentration where the FS grows to include $4f$ electrons.

We probed the magnetism of CeNiAsO through magnetic neutron scattering on the NOMAD and POWGEN diffractometers [14, 15] and on the SEQUOIA [16] spectrometer at the Spallation Neutron Source. For complementary real space information we used muon spin rotation (μ SR) at the M15 beam line at TRIUMF. Specific heat measurements were conducted on a 14 Tesla Quantum Design PPMS with a dilution fridge insert.

Fig. 1(a) shows the tetragonal structure of CeNiAsO where magnetism is associated with Ce^{3+} sandwiching a square lattice of oxygen. The structure and the single phase nature of the sample was ascertained by Rietveld refinement of high resolution neutron diffraction data (see SI). The specific heat data in Fig. 3(d) show shoulder-like anomalies indicating two second order phase transitions at $T_{N1} = 9.0(3)$ K and $T_{N2} = 7.6(3)$ K. The inferred critical temperatures are consistent with previously published specific heat data with sharper peaks indicating higher purity[12]. The rounded maxima shift towards lower T and approach each other in a field of $\mu_0 H = 14$ T as for two distinct antiferromagnetic phases.

To determine their nature, we use zero field μ SR in the longitudinal configuration [17, 18]. Fig. 2 shows muon spin precession indicative of a well defined static internal field for $T < T_{N1}$. A qualitative change in the μ SR profile for $T < T_{N2}$ indicates two distinct magnetic phases. For $T_{N2} < T < T_{N1}$, muons sample the broad spectrum of local fields generated by an incommensurate SDW [19]. For $T < 6$ K, the signal is oscillatory (Fig. 2 (b)) with a beating pattern that indicates two distinct precession frequencies and commensurate magnetism. These patterns can be fitted by magnetic structures

that are consistent with the neutron data and a single crystallographic muon stopping site.

We determined the fundamental magnetic wave vector and spin polarization through neutron diffraction. Weak magnetic peaks are apparent at $T = 2$ and 8 K after subtracting data at $T = 15$ K (Fig. 2 (c-d)). At $T = 2$ K, the difference pattern shows several resolution limited peaks. The peak with the lowest wave vector transfer $Q \approx 0.77 \text{ \AA}^{-1}$ can be indexed as $\mathbf{Q}_m = (0.5, 0, 0)$. Magnetic neutron diffraction probes spin polarization perpendicular to wave vector transfer so this indexing implies spin components along \mathbf{b} and/or \mathbf{c} . Upon warming to 8 K $< T_{N1}$, the absence of this first peak is indicative of a longitudinal spin density wave (SDW) polarized along \mathbf{a} . The width of the intensity maxima for $T = 8$ K and $Q \approx 1.1 \text{ \AA}^{-1}$ in Fig. 2 (c) exceeds the instrumental Q -resolutions. The incommensurability indicated by μ SR can account for this. The magnetic signal at 8 K is however quite weak and since there is no energy resolution, inelastic magnetic scattering may also contribute to the broadened peaks, particularly near the polarization suppressed \mathbf{Q}_m peak. The diffraction data thus do not permit a unique determination of the spin structure for $T_{N2} < T < T_{N1}$. The combination of muon, specific heat, and elastic/inelastic neutron data, however, does allow an accurate determination of both structures.

Using Kovalev notation [20, 21], the reducible magnetic representation associated with $\mathbf{k} = (\mu 00)$ decomposes into three two-dimensional irreducible representations (IR): $\Gamma_{mag} = 2\Gamma_1^{(2)} + \Gamma_2^{(2)}$ with 6 Basis Vectors (BVs) (Table S2). Landau theory allows only one IR for each of the two second order phase transitions. Below T_{N1} , BVs $\psi(4)$ and $\psi(6)$ of Γ_1 depict a spin structure with

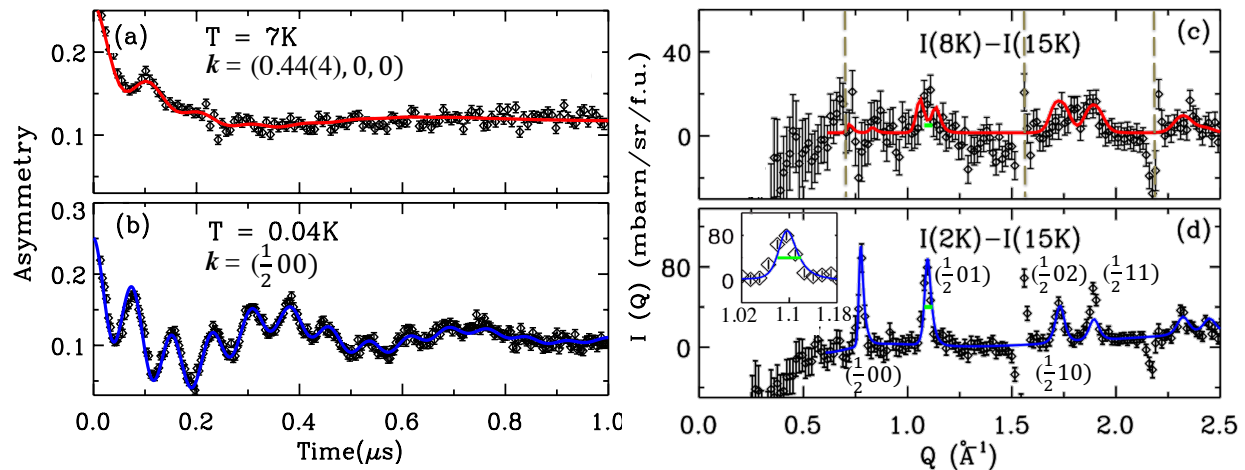


FIG. 2: (a-b) Zero-field longitudinal configuration μ SR spectra at $T = 7$ K and 0.05 K. The colored lines were calculated for the magnetic structures of Fig. 1. (c-d) Diffraction patterns collected at $T = 2$ K and 8 K on NOMAD, after subtracting $T = 15$ K data as a measure of nuclear diffraction. Red and blue lines correspond to the spin configurations in Fig. 1. The grey dashed lines in (c) mark the nuclear Bragg positions, where thermal expansions gives rise to a peak-derivative anomaly. In (d) the horizontal green bar at $Q = 1.1 \text{\AA}^{-1}$ indicates the instrument resolution of 0.04\AA^{-1} as detailed in the inset.

moments along \mathbf{a} . Adding $\psi(3)$ and $\psi(5)$ allows for moments along \mathbf{c} . Below T_{N2} , we can account for the diffraction pattern in Fig. 2 (d) by adding $\psi(1)$ and $\psi(2)$ of Γ_2 . The best fit corresponds to a reduced $\chi^2 = 1.95$ and a staggered moment $\langle m \rangle = 0.37(5) \mu_B/\text{Ce}$ that is canted by $\varphi \approx 36(6)^\circ$ to the \mathbf{a} axis (Fig. 1 (c)). While allowed by symmetry, the diffraction data place a limit of $0.06 \mu_B$ on any \mathbf{c} -component of the staggered moment.

μ SR, which probes magnetism in real space, offers an independent assessment of the proposed structures. We find a consistent description of the precession data with the muon stopping site $(\frac{1}{4}, \frac{3}{4}, z_\mu)$ in Fig.1 (a). The fitting analysis described below yields $z_\mu = 0.1471(3)$ ($=z_{\text{Ce}}$), close to the preferred distance of muons from O^{2-} [22]. This location is also favored considering the electrostatic potential-energy map for CeFeAsO [23]. The observation of two muon precession frequencies suggests two magnetically inequivalent muon sites (see Fig.1 (b-c)). The asymmetry pattern $P_\mu^z(t)$ can be fitted to equation S1 wherein the magnetic field distribution function $\rho_i(B)$ is calculated directly from the spin structures. For the low T commensurate state, $\rho_i(B)$ consists of two delta functions corresponding to the magnetic field at each of the two magnetically inequivalent (but crystallographically equivalent) muon sites. The best fit is obtained with moment $m = 0.37(2)\mu_B$ and rotation angle $\varphi = 36(7)^\circ$, which is in excellent agreement with the Rietveld refinement of neutron diffraction. For the high T incommensurate state, $\rho_i(B)$ is continuous: The incommensurate nature of the spin structure ensures every muon site, though crystallographically equivalent, is magnetically unique and contributes a distinct precession frequency. The best fit leads to an incommensurate wave vector

$\mathbf{k}=(0.44(4),0,0)$, $m_a = 0.27(6)\mu_B$, and $m_c = 0.08(3)\mu_B$. The corresponding calculated muon asymmetry and neutron diffraction are in Fig. 2 (a)&(c). A small component of m_c implies this is a magnetic cycloid. The corresponding lack of inversion symmetry could have interesting consequences for electronic transport. However, since $m_c \ll m_a$ we retain the terminology of a longitudinal SDW. In summary, the spin structures for two ordered states – a longitudinal SDW (Fig. 1 (b), Fig. S4) and a commensurate coplanar structure (Fig. 1 (c)) – account for both neutron and μ SR data.

For context we examine the $4f$ electron crystal field excitations through inelastic magnetic neutron scattering (Fig. 4(a-e)). At $T = 7$ K, the intensities of modes at $E \approx 10$ meV, 30 meV and 40 meV rise with Q^2 and are observed both for CeNiAsO and non-magnetic LaNiAsO and so must be vibrational[27]. In the difference data $\tilde{I}(Q, E)$ and $\tilde{I}(E)$ (Fig. 4 (c-e)), we associate the two broad modes at $E_1 \approx 18(3)$ meV and $E_2 \approx 70(8)$ meV with magnetic excitations because their intensity decreases with Q as the $4f$ formfactor. In the tetragonal environment of Ce^{3+} , the $J = \frac{5}{2}$ multiplet splits into three Kramer's doublets. The two magnetic modes are correspondingly assigned to crystal-field-like excitations from the ground state (GS) to two excited doublets. At $T = 200$ K population of the excited state yields a broad mode at $50 \text{ meV} \approx E_2 - E_1$, which arises from excitations between the excited doublets. Finally we observe a sharp mode at $E_0 \approx 2$ meV within the AFM ordered state (inset, Fig.4 (d)). In the language of CEF theory, this is an intra-doublet transition driven to inelasticity by the molecular exchange field. As expected for a strongly correlated solid, the crystal field excitations measured for a powder sample are broadened by damping and

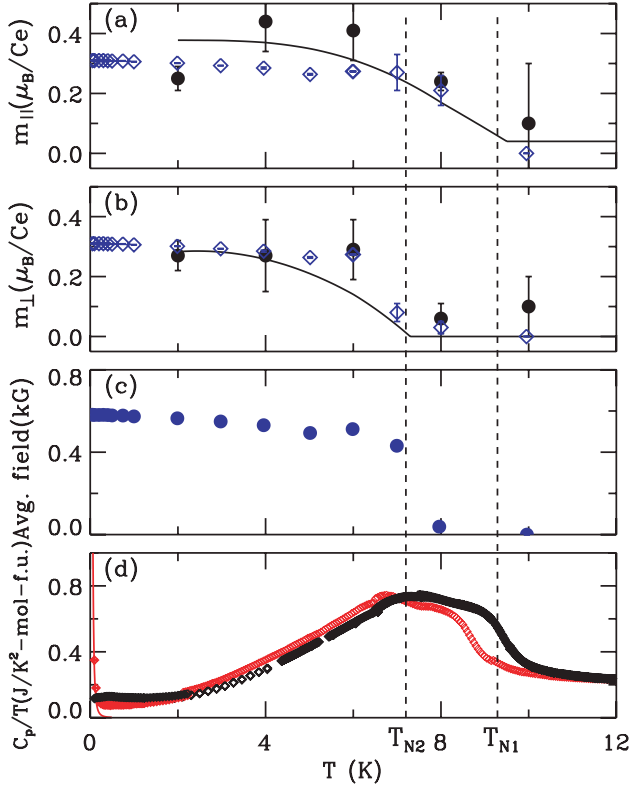


FIG. 3: Temperature dependence of (a) the longitudinal (m_a) and (b) the transverse moments (m_c for high T and m_b for low T phase). Black dots were extracted from Rietveld fits to neutron diffraction data. The 2 K and 8 K data points were averaged over two chopper settings. Blue diamonds were inferred from μSR fits. The solid lines are guides to the eye. (c) Temperature dependence of the averaged static field. (d) Specific heat C_p/T in zero field and for $\mu_0 H = 14$ T. The upturn in C_p/T at 14 T is due to the nuclear spin contributions as indicated by the solid red line.

dispersion, leading to the half width at half maximum (HWHM) of $\Gamma_1 = 13$ meV and $\Gamma_3 = 24$ meV. Fitting to Lorentzian spectral functions leads to HWHM of $\Gamma_0 = 2$ meV that is comparable to the Kondo temperature $T_K = 15(5)$ K inferred from thermo-magnetic data [12].

Given these broad modes, a local moment crystal field model cannot be comprehensive but it provides a useful starting point. As detailed in the SI, we carried out a global fit of a symmetry-constrained crystal field model to the normalized scattering data $\tilde{I}(E)$ at $T = 7$ K and 200 K. After optimizing the crystal field parameters a molecular exchange field and three transition specific relaxation rates, Fig. 4(d-e) shows a consistent description of data from two instrumental configurations and two temperatures is achieved. The model also accounts for the temperature dependent susceptibility data. Consistent with the easy plane (ab plane) character of the ordered states, the GS wave function is $|\pm \frac{1}{2}\rangle$ (Γ_7).

As indicated in the DFT FS plot (Fig. 1 (d)),

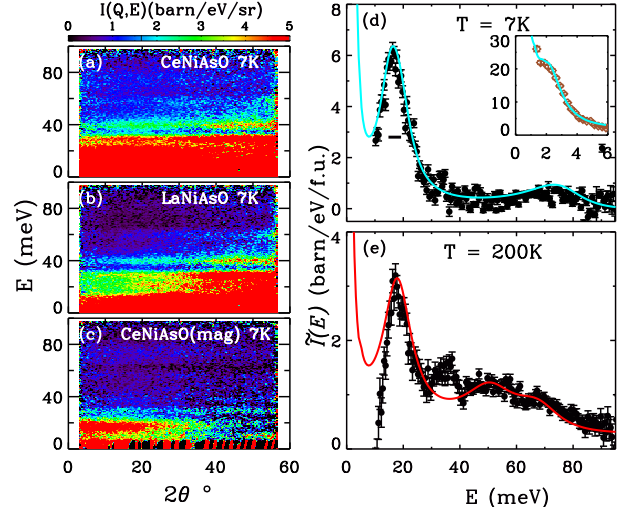


FIG. 4: Normalized inelastic spectrum with incident energy $E_i = 100$ meV (black dots) for (a) CeNiAsO and (b) the non-magnetic reference LaNiAsO. (c) The $T = 7$ K difference spectrum: $\tilde{I}(Q, E) = I_{Ce} - rI_{La}$ where $r = \sigma_{\text{CeNiAsO}}/\sigma_{\text{LaNiAsO}}$. (d-e) Momentum-integrated scattering at $T = 7$ K and 200 K by using the method in Ref. [24–26]. The horizontal black bar indicates energy resolution. The inset in (d) shows a magnetic excitation at 2 meV in the ordered state with $E_i = 50$ meV (brown dots). The cyan and red solid lines were calculated for the crystal field model described in the text.

the ordering wave vector $\mathbf{k} = (0.44(4), 0, 0)$ satisfies a nesting condition. This suggests the ordered state for $T_{N2} < T < T_{N1}$ should be classified as a SDW [28–32]. It is common for incommensurate (IC) magnets to undergo a longitudinal to transverse spin reorientation transition that reduces the modulation in the magnitude of the dipole moment per unit cell while sustaining the IC modulation [30, 33]. The situation is different for CeNiAsO, which not only develops transverse magnetization but also becomes commensurate for $T < T_{N2}$. To arrive at the spin structure in Fig. 1 (c) from the commensurate version of Fig. 1 (b) involves counter-rotating the upper and lower AFM layers of a CeO sandwich (Fig. 1 (a)) by $\varphi = 36^\circ(5)$ around \mathbf{c} . While inter-layer bi-linear interactions vanish at the mean field level for $\mathbf{k} = (0.5, 0, 0)$ type order, inter-layer bi-quadratic interactions[34, 35] give rise to a term in the free energy of the form $(m^2 \cos 2\varphi)^2$ that can favor $\varphi = 45^\circ$ for a commensurate structure only. As m grows upon cooling this term can be expected to induce both the IC to commensurate transition and the symmetry breaking transverse magnetization at T_{N2} .

This brings us to the character of magnetism in $\text{CeNiAs}_{1-x}\text{P}_x\text{O}$. Upon cooling, CeNiAsO passes from Fermi liquid to IC SDW to commensurate non-collinear order in two second order phase transitions. P doped samples that we examined ($\text{CeNiAs}_{1-x}\text{P}_x\text{O}$ for $x > 0.1$)

all show the characteristic μ SR oscillation associated with IC magnetism (Fig.2 (a)) down to 50 mK. This indicates the commensurate state is limited to a low T , low x pocket (Fig. 1 (d)) and the initial instability of the strongly correlated Fermi liquid in $\text{CeNiAs}_{1-x}\text{P}_x\text{O}$ is to an IC SDW. An important open question is whether the characteristic wave vector of the SDW evolves with x or continues to be associated with the small FS as for $x = 0$.

We thank Gerald Morris, Bassam Hitti, and Iain McKenzie for μ SR beam line support, Sky Cheung and Yipeng Cai for assistance during the μ SR experiment, and Allen Scheie for useful discussions on crystal field analysis. This research was funded by the US Department of Energy, office of Basic Energy Sciences, Division of Material Sciences and Engineering under grant DE-SC0019331 and by the Gordon and Betty Moore foundation through GBMF4532. The research at ORNL's Spallation Neutron Source was sponsored by the Scientific User Facilities Division, Office of Basic Energy Sciences, U.S. Department of Energy. Activities at Columbia and TRIUMF were supported by NSF DMR-1436095 (DMREF) and DMR-1610633, and the REIMEI project of Japan Atomic Energy Agency.

* Electronic address: shanwu@berkeley.edu

- [1] S. Doniach, *Physica B+C* **91**, 231 (1977).
- [2] P. Gegenwart, Q. Si, and F. Steglich, *Nature Phys.* **4**, 186 (2008).
- [3] P. Coleman and A. J. Schofield, *Nature* **433**, 226 (2005).
- [4] L. Jiao, Y. Chen, Y. Kohama, D. Graf, E. D. Bauer, J. Singleton, J.-X. Zhu, Z. Weng, G. Pang, T. Shang, et al., *Proceedings of the National Academy of Sciences* **112**, 673 (2015).
- [5] T. Park, F. Ronning, H. Q. Yuan, M. B. Salamon, R. Movshovich, J. L. Sarrao, and J. D. Thompson, *Nature* **440** **7080**, 65 (2006).
- [6] H. Shishido, R. Settai, H. Harima, and Y. ?nuki, *Journal of the Physical Society of Japan* **74**, 1103 (2005).
- [7] C. Stock, C. Broholm, F. Demmel, J. Van Duijn, J. W. Taylor, H. J. Kang, R. Hu, and C. Petrovic, *Phys. Rev. Lett.* **109**, 127201 (2012).
- [8] S. Friedemann, T. Westerkamp, M. Brando, N. Oeschler, S. Wirth, P. Gegenwart, C. Krellner, C. Geibel, and F. Steglich, *Nature Physics* **5**, 465 (2009), ISSN 1745-2473.
- [9] S. Paschen, T. Lhmann, S. Wirth, P. Gegenwart, O. Trovarelli, C. Geibel, F. Steglich, P. Coleman, and Q. Si, *Nature* **432**, 881885 (2004), ISSN 0028-0836.
- [10] S. Paschen, T. Lühmann, S. Wirth, P. Gegenwart, O. Trovarelli, C. Geibel, F. Steglich, P. Coleman, and Q. Si, *Nature* **432**, 881 (2004).
- [11] S. Friedemann, N. Oeschler, S. Wirth, C. Krellner, C. Geibel, F. Steglich, S. Paschen, S. Kirchner, and Q. Si, *Proc. National Academy of Sciences* **107**, 14547 (2010).
- [12] Y. Luo, H. Han, H. Tan, X. Lin, Y. Li, S. Jiang, C. Feng, J. Dai, G. Cao, Z. Xu, et al., *J. Phys.: Cond. Matter* **23**, 175701 (2011).
- [13] Y. Luo, L. Pourovskii, S. Rowley, Y. Li, C. Feng, A. Georges, J. Dai, G. Cao, Z. Xu, Q. Si, et al., *Nature Mat.* **13**, 777 (2014).
- [14] J. Neufeind, M. Feygenson, J. Carruth, R. Hoffmann, and K. K. Chipley, *Nuclear Instruments and Methods in Phys. Res. B: Beam Interactions with Materials and Atoms* **287**, 68 (2012), ISSN 0168-583X.
- [15] A. Huq, J. P. Hodges, O. Gourdon, and L. Heroux, *Z. Kristallogr. Proc* **1**, 127 (2011).
- [16] G. E. Granroth, A. I. Kolesnikov, T. E. Sherline, J. P. Clancy, K. A. Ross, J. P. C. Ruff, B. D. Gaulin, and S. E. Nagler, *J. Phys.: Conf. Series* **251**, 012058 (2010).
- [17] A. Schenck, *Muon Spin Rotation Spectroscopy: Principles and Applications in Solid State Physics* (Bristol: Adam Hilger, 1985).
- [18] S. Lee, S. Kilcoyne, and R. Cywinski, *Chemistry and Materials, Proceedings of the 50th Scottish University Summer School in Physics* **51** (1998).
- [19] Y.J.Uemura, *Muon Science* pp. 85–114 (1999).
- [20] O. V. Kovalev, *Irreducible Representations of the Space Groups* (Routledge, 1965).
- [21] A. Wills, *Physica B: Cond. Matter* **276**, 680 (2000).
- [22] P. Meier, J. Chappert, and R. Grynspan, *Muons and pions in materials research* (1984).
- [23] H. Maeter, H. Luetkens, Y. G. Pashkevich, A. Kwadrin, R. Khasanov, A. Amato, A. A. Gusev, K. V. Lamonova, D. A. Chervinskii, R. Klingeler, et al., *Phys. Rev. B* **80**, 094524 (2009).
- [24] A. P. Murani, *Phys. Rev. B* **28**, 2308 (1983).
- [25] A. P. Murani, *Phys. Rev. B* **50**, 9882 (1994).
- [26] E. A. Goremychkin and R. Osborn, *Phys. Rev. B* **47**, 14280 (1993).
- [27] V. F. Sears, *Neutron News* **3**, 26 (1992).
- [28] W. Bao, P. G. Pagliuso, J. L. Sarrao, J. D. Thompson, Z. Fisk, J. W. Lynn, and R. W. Erwin, *Phys. Rev. B* **62**, R14621 (2000).
- [29] C. Stock, J. A. Rodriguez-Rivera, K. Schmalzl, E. E. Rodriguez, A. Stunault, and C. Petrovic, *Phys. Rev. Lett.* **114**, 247005 (2015).
- [30] E. Fawcett, *Rev. Mod. Phys.* **60**, 209 (1988).
- [31] Y. Sidis, M. Braden, P. Bourges, B. Hennion, S. NishiZaki, Y. Maeno, and Y. Mori, *Phys. Rev. Lett.* **83**, 3320 (1999).
- [32] I. I. Mazin and D. J. Singh, *Phys. Rev. Lett.* **82**, 4324 (1999).
- [33] G. Lawes, A. B. Harris, T. Kimura, N. Rogado, R. J. Cava, A. Aharony, O. Entin-Wohlman, T. Yildirim, M. Kenzelmann, C. Broholm, et al., *Phys. Rev. Lett.* **95**, 087205 (2005).
- [34] Y. Akagi, M. Udagawa, and Y. Motome, *Phys. Rev. Lett.* **108**, 096401 (2012).
- [35] S. Hayami and Y. Motome, *Phys. Rev. B* **90**, 060402 (2014).
- [36] T. McQueen, T. Klimczuk, A. Williams, Q. Huang, and R. Cava, *Physical Review B* **79**, 172502 (2009).
- [37] J. Rodriguez-Carvajal, in *Satellite meeting on powder diffraction of the XV congress of the IUCr* (Toulouse, France:[sn], 1990), vol. 127.
- [38] J. Zhao, Q. Huang, C. de La Cruz, S. Li, J. Lynn, Y. Chen, M. Green, G. Chen, G. Li, Z. Li, et al., *Nature Mat.* **7**, 953 (2008).
- [39] G. Kresse and J. Furthmuller, *J. Comp. Materials* **6**, 15 (1996).
- [40] G. Kresse, *Phys. Rev. B* **54**, 11169 (1996).

- [41] G. Kresse and J. Hafner, Phys. Rev. B **43**, 558 (1993).
- [42] C. Kittel, *Introduction to Solid State Physics* (Wiley, 2005).
- [43] E. Heltemes and C. Swenson, J. Chem. Phys. **35**, 1264 (1961).
- [44] C.D.Bredl, S.Horn, and F. Steglich, Phys. Rev. Lett. **52**, 22 (1984).
- [45] K. W. H. Stevens, Proc. Phys. Soc. A **65**, 209 (1952).
- [46] S. Lovesy, *Theory of magnetic neutron and photon scattering* (1989).
- [47] J. Jensen, J. Magn. Magn. Mater. **29**, 47 (1982).
- [48] See Supplementary Material for the following information: the sample synthesis [36], details in the Rietveld refinement [37, 38], details in the DFT calculation [39–41], analysis of Schottky anomaly [42–44] in the low-T specific heat, crystal field analysis and corresponding magnetic susceptibility calculation [45–47].

Supplementary Material for ‘Incommensurate magnetism near quantum criticality in CeNiAsO’

Shan Wu^{1,2*}, W. Adam Phelan¹, L. Liu³, J. R. Morey¹, J. A. Tutmaher¹, J. C. Neufeind⁴, Ashfia Huq⁵, Matthew B. Stone⁵, M. Feynson⁶, David W. Tam⁷, Benjamin A. Frandsen⁸, Benjamin Trump⁹, Cheng Wan¹, S. R. Dunsiger¹⁰, T. M. McQueen^{1,11}, Y. J. Uemura³, and C. L. Broholm^{1,11,12}
(Dated: June 18, 2021)

In support of the main text, the following supplementary information is provided: (1) synthesis details and nuclear structure refinement from neutron diffraction; (2) details about the neutron measurements, μSR experiments, and DFT calculation; (3) details and discussion about an additional low temperature T_3 anomaly in specific heat; (4) crystal fields analysis of inelastic neutron scattering data.

SYNTHESIS METHOD AND NUCLEAR STRUCTURE DETERMINATION

Synthesis method

Samples of CeNiAsO were synthesized by pelletizing CeO₂ (Alfa Aesar, 99.99 %), NiAs (pre-fired), and Ce metal (Alfa Aesar, 99.8 %) stoichiometrically, sealing the pellet in an evacuated-fused silica tube. The reaction ampoule was placed in a furnace and heated to 1000 °C at a rate of 100 °C/hr. The temperature was held constant at 1000 °C for 5 hours. The ampoule was then allowed to furnace cool to room temperature.

Phosphorous doped samples were synthesized following the procedure described in Ref. [1]. For each sample, CeO₂, Ni₅P₄ (pre-fired), Ce metal, purified and dried P, and NiAs (pre-fired) were mixed and ground thoroughly and stoichiometrically to CeNiAs_{1-x}P_xO_{0.98}. The pressed pellet was placed in a dry alumina crucible and sealed into an evacuated ampoule. The ampoule was heated from 750 °C to 1050 °C over 1 hour and held at 1050 °C for 5 hours. After cooling to room temperature in the furnace, the sample was re-grounded and re-pressed with excess of 2 % P to account for vaporization during pre-reaction. The sample was then pressed into a pellet again and placed in the same alumina crucible into a new ampoule. The ampoule was sealed into a larger ampoule backfilled with 1/3 atm Ar (99.99%). This ampoule was placed directly into a furnace that was pre-heated to 1300 °C and it remained there for 8-12 hours. After cooling on the bench top, such heating to 1300 °C and bench-top cooling was repeated 2-4 times with intermediate grinding, until the starting materials were no longer visible in powder x-ray diffraction (details later). The entire synthesis was conducted in an argon atmosphere. The sample was exposed to air less than 10 mins during each regrind/reheat/reseal cycle.

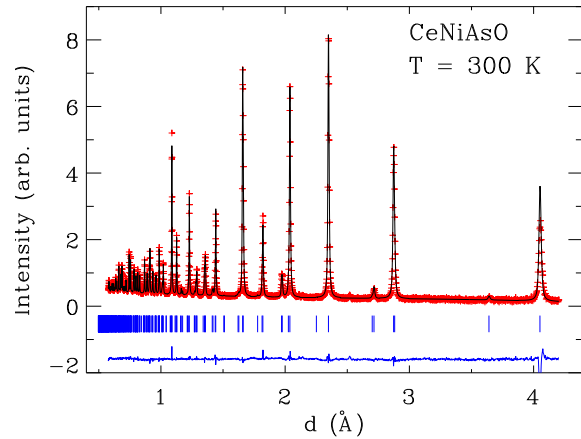


FIG. S1: Rietveld refinement of neutron diffraction that establishes the chemical structure of CeNiAsO at $T = 300$ K. Red dots are from POWGEN in the year of 2013 with a total proton charge of $3.3 \cdot 10^{-3}$ Ah. The black curve is the Rietveld profile based on the tetragonal $P4/nmm$ spacegroup. The blue trace is the difference between the measurements and the Rietveld profile.

Nuclear structure determination

The structure of CeNiAsO was determined by Rietveld refinement of $T = 300$ K data acquired on POWGEN (Fig. S1), using *Fullprof*[2]. The data were refined in the tetragonal space group $P4/nmm$. The corresponding atomic positions and lattice parameters are listed in Table S1 (Bragg R-factor = 5.37). The inferred structure is consistent with powder x-ray diffraction (XRD) refinement. Laboratory powder x-ray diffraction data were collected using a Bruker D8 Focus diffractometer equipped with Cu $K\alpha$ radiation and a LynxEye detector. Phase identification and phase purity checks were conducted through Rietveld refinement. A 4 hours XRD measurement found only 0.75% by volume of CeNi₂As₂ as the only detectable impurity phase. A pair distribution analysis of the NOMAD data found no evidence of a local structural distortion as in CeFeAsO [3]. In

TABLE S1: $T = 300$ K atomic positions for CeNiAsO with space group $P4/nmm$ determined by the Rietveld refinement of neutron powder diffraction data. The corresponding lattice parameters are $a = 4.0621(1)$ Å and $c = 8.1058(3)$ Å.

Atom	Site	x	y	z	U_{iso} (Å)
Ce	2c	1/4	1/4	0.1471(3)	0.0070(5)
Ni	2b	3/4	1/4	1/2	0.0120(3)
As	2c	1/4	1/4	0.6439(3)	0.0081(4)
O	2a	3/4	1/4	0	0.0056(4)

$R_{wp} = 7.07, R_p = 10.3, R_{exp} = 2.06, \chi^2 = 10.9$

TABLE S2: The 6 basis vectors associated with magnetic structures that transform according to irreducible representations with propagation vector $\mathbf{k} = (\frac{1}{2}, 0, 0)$, using Kovalev notation as implemented in SARAh.

IR	BV	Atom1 $m_x m_y m_z$	Atom2 $m_x m_y m_z$
Γ_2	$\psi(1)$	0 0 0	0 -1 0
	$\psi(2)$	0 1 0	0 0 0
Γ_1	$\psi(3)$	0 0 1	0 0 0
	$\psi(4)$	0 0 0	1 0 0
	$\psi(5)$	0 0 0	0 0 -1
	$\psi(6)$	1 0 0	0 0 0

CeNiAs $_{1-x}$ P $_x$ O samples with nominal values of $x=0.2, 0.3, 0.4,$ and $0.5,$ we found $x = 0.19(1), 0.29(1), 0.33(1)$ and $0.49(1)$ respectively. These values were consistent with SEM/EDX measurements.

EXPERIMENTAL DETAILS

Elastic scattering

Neutron diffraction was carried out using the Nanoscale Ordered Materials Diffractometer (NOMAD) at the Oak Ridge National Laboratories (ORNL). Data were collected with a total proton charge of 4.5 mAh at $T = 2$ K, 8 K, and 15 K, with a 30 Hz bandwidth (BW) chopper, admitting a wavelength band from 0.1 Å to 3 Å in the first frame. Temperature dependence measurements were obtained with a proton charge of 2 mAh each from 2 K to 10 K in 2 K steps, with 60 Hz pulse rate and admitting a wavelength band from 3 Å to 6 Å. We used a vanadium sample can and corrected for background through separate measurements of the empty instrument and an empty sample can. Diamond scans were used for calibration purposes. Absolute unites for magnetic diffraction were obtained by scaling to nuclear Bragg intensities.

Inelastic scattering

Inelastic neutron scattering was performed using the SEQUOIA Fermi chopper spectrometer at SNS, ORNL.

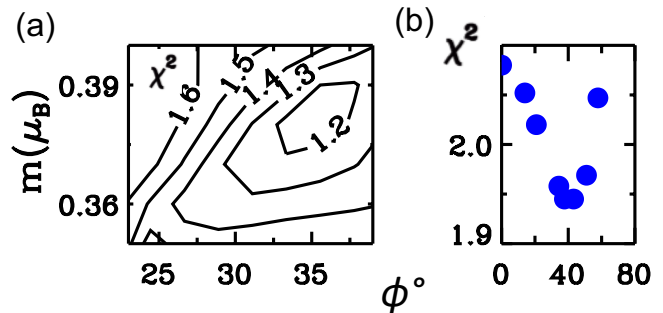


FIG. S2: Contour plot of the reduced χ^2 for μ SR fits (a) and the reduced χ^2 versus φ for Rietveld fits to powder neutron diffraction data (b) below T_{N2} . The rotation angle of magnetic moment φ is defined as follows: $\tan\varphi = m_{\perp\mathbf{k}}/m_{\parallel\mathbf{k}}$.

We used a multi-sample exchange system to mount CeNiAsO ($m \approx 2.31$ g) and its non-magnetic analogy LaNiAsO ($m \approx 2.32$ g) in two thin cylindrical aluminum cans, sealed under 1 atm of ^4He . The sample was cooled to $T = 7$ K using a close-cycle cryostat. To optimize intensity and resolution, we used two configurations with different incident energy E_i : 1) Fermi fine chopper frequency $\nu_2 = 360$ Hz and T_0 chopper frequency $\nu_0 = 90$ Hz for $E_i = 50$ meV; 2) Fermi sloppy chopper frequency $\nu_1 = 240$ Hz and $\nu_0 = 60$ Hz for $E_i = 100$ meV. The corresponding Full Width at Half Maximum (FWHM) elastic energy resolutions ΔE were 1 meV and 5.7 meV respectively.

μ SR experiment

We performed zero field (ZF) μ SR with the detectors in the longitudinal configuration on the M15 beam line at Canada's national laboratory for particle and nuclear physics (TRIUMF). The samples were mounted using Apiezon N grease, covered with Alfa Aesar 0.025 mm thick silver foil, and cooled in a dilution refrigerator to 0.04 K.

The asymmetry pattern $P_{\mu}^z(t)$ can be fitted to the following expression:

$$A_s \sum_i \left(\frac{2}{3} e^{-\lambda_i t} \int \rho_i(B) \cos(\gamma_{\mu} B t) dB + \frac{1}{3} e^{-\lambda_s t} \right) + A_{bg} e^{-\lambda_{bg} t} \quad (\text{S1})$$

Here A_s is the total asymmetry stopped in the sample at $t = 0$. We assume equal weight for the two magnetically distinct muon sites (ratio = 1.0(2)). $\rho_i(B)$ is the magnetic field distribution at the muon site i . λ_i and λ_s are the rapid transverse and slow longitudinal rate respectively, and $\gamma_{\mu}/2\pi = 135.53$ MHz T^{-1} is the gyromagnetic ratio of the muon. The last term accounts for muons stopped beyond the sample.

We calculated the internal field distribution $\rho_i(B)$ on the putative muon interstitial sites and spin configurations for comparison to the μ SR data. For

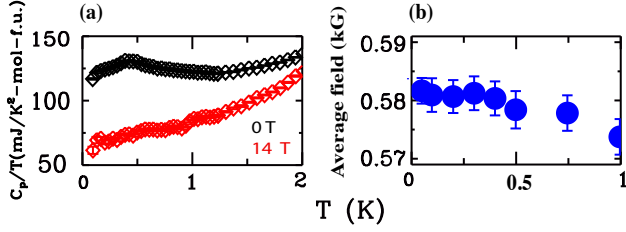


FIG. S5: CeNiAsO: (a) specific heat data acquired in a PPMS plotted as C_p/T for temperatures below 2 K, after subtracting the calculated hyperfine nuclear spin contributions for zero field and 15 T. (b) Extracted average field below 1 K from muon spin rotation measurement.

sensitivity to an applied fields (4) an anomaly associated with a second phase in the sample.

CRYSTAL FIELD ANALYSIS

The crystal field inelastic spectrum (Fig. ?? (c)-(e)) was obtained from inelastic neutron scattering data acquired on SEQUOIA after subtracting scaled data from the non-magnetic reference sample LaNiAsO and normalizing based on Bragg diffraction. In the PM phase the Hamiltonian is expressed in terms of Stevens operators [30] that are allowed by the point group symmetry and account for the observed CEF modes. In the ordered state, a mean field description of inter-site interactions adds a molecular field term. The inelastic spectrum collected with incident energy $E_i = 50$ meV in Fig 4. (d-e) is shown in the Fig. S6. The $E = 30$ meV mode in Fig. S6(c) is the remnant of a phonon mode that is more apparent in Fig. S6(a) and Fig. S6(b). The difference of momentum-integrated scattering $\tilde{I}(E)$ in the Fig. 4 (e) is obtained by subtracting LaNiAsO data from CeNiAsO data. Broad CEF excitations and one sharp mode that appears in the ordered state can be reproduced by the following phenomenological model. The Ce atoms are located at the $2c$ crystallographic site which has C_{4v} point group symmetry. In the paramagnetic state, the CEF Hamiltonian that operates on the ground state J -multiplet can be written as:

$$\hat{H}_{CEF} = B_2^0 \hat{O}_2^0 + B_4^0 \hat{O}_4^0 + B_4^4 \hat{O}_4^4. \quad (S3)$$

Here B_l^m are the pre-factors of Stevens operators (denoted CEF parameters here) and \hat{O}_l^m are the Stevens equivalent operators [10]. In the ordered state, the contribution of a molecular exchange field was added to the CEF Hamiltonian \hat{H}_{CEF} as follows:

$$\hat{H} = \hat{H}_{CEF} - g_j \mu_B \mathbf{B}_{\text{eff}} \cdot \mathbf{J}. \quad (S4)$$

The cross section for unpolarized neutron scattering from a polycrystalline sample arising from transitions

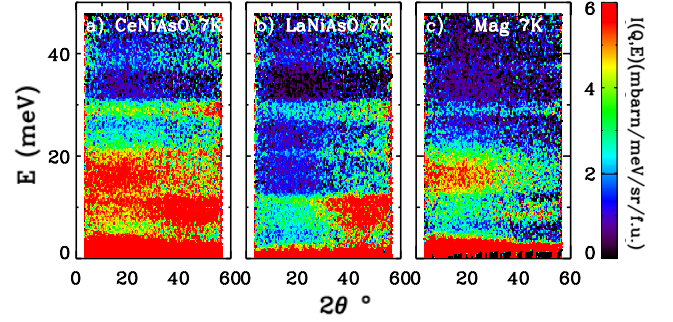


FIG. S6: Normalized inelastic neutron scattering cross section acquired with incident energy $E_i = 50$ meV for (a) CeNiAsO and (b) the non-magnetic reference LaNiAsO. (c) The difference data, which is predominantly magnetic neutron scattering.

from state $|i\rangle$ to $|j\rangle$ can be expressed as follows [11]:

$$\frac{d^2\sigma}{d\Omega dE} = N \frac{k_f}{k_i} \left| \frac{1}{2} g_j r_0 F(\mathbf{Q}) \right|^2 \times \frac{2}{3} \sum_{i,j,\alpha} p_i |\langle i | J_\alpha | j \rangle|^2 \delta(E_i - E_j + \hbar\omega) \quad (S5)$$

We replaced the Dirac delta function with a unity normalized Lorentzian function with Half Width at Half Maximum (HWHM) $\Gamma_n = 13(2), 23(3), 24(1)$ meV for the three CEF modes and $\Gamma_0 = 2.0(2)$ meV for the sharp low energy mode. The width of three modes are much broader than the instrumental resolution even under the $E_i = 50$ meV configuration. The dispersive bands of hybridized $4f$ and conduction electrons may account for the broadening. The molecular field term $\mathbf{B}_{\text{eff}} \cdot \mathbf{J}$ can be further simplified as $B_{\text{eff}} J_{\parallel}$, considering an in-plane effective field. Three CEF parameters and one molecular field parameter were obtained by fitting to the T -dependent magnetic neutron scattering spectra. The corresponding fitting parameters and wave functions are listed in Table S3 - S5 for the PM and ordered states. The schematic crystal field scheme is displayed in Fig. S7. The difference in B_2^0 and B_4^4 between the two measurements is within error bars. The sign change for B_4^0 could result from a multipolar mean field.

TABLE S3: The parameters obtained from fitting a crystal field model to inelastic neutron scattering data. B_2^0 , B_4^0 , B_4^4 are coefficients of Steven operators in the crystal field Hamiltonian. B_{eff} is the effective molecular field within the ordered state for $T = 2$ K.

T (K)	B_2^0 (meV)	B_4^0 (meV)	B_4^4 (meV)	B_{eff} (T)
7	3.1(1)	0.07(1)	1.1(1)	1.7(2)
200	2.3(1)	-0.09(4)	0.9(1)	-

To verify the scheme of crystal field, we also measured the magnetic susceptibility of a polycrystalline sample. The data was collected with external field $H = 1000$ Oe as shown in Fig. S8. The magnetic susceptibility χ^α

TABLE S4: Wave functions considering the effective molecular field at $T = 7$ K. The three doublets are divided into 6 non-degenerate singlets. The \pm sign prior to the coefficient indicates summation over each component of angular moment.

ψ_5	$\mp 0.641 \pm \frac{5}{2} \rangle \pm 0.298 \pm \frac{3}{2} \rangle \mp 0.009 \pm \frac{1}{2} \rangle$
ψ_4	$-0.648 \pm \frac{5}{2} \rangle - 0.281 \pm \frac{3}{2} \rangle + 0.008 \pm \frac{1}{2} \rangle$
ψ_3	$\pm 0.035 \pm \frac{5}{2} \rangle \pm 0.052 \pm \frac{3}{2} \rangle \mp 0.704 \pm \frac{1}{2} \rangle$
ψ_2	$-0.043 \pm \frac{5}{2} \rangle + 0.079 \pm \frac{3}{2} \rangle - 0.701 \pm \frac{1}{2} \rangle$
ψ_1	$-0.278 \pm \frac{5}{2} \rangle + 0.643 \pm \frac{3}{2} \rangle + 0.091 \pm \frac{1}{2} \rangle$
ψ_0	$\pm 0.296 \pm \frac{5}{2} \rangle \pm 0.639 \pm \frac{3}{2} \rangle \pm 0.062 \pm \frac{1}{2} \rangle$

TABLE S5: Wave functions for three doublets associated with Ce^{3+} in CeNiAsO inferred from inelastic neutron at 200 K.

Energy (meV)	Doublet wave function
70(8)	$0.7518 \pm \frac{5}{2} \rangle + 0.6593 \mp \frac{3}{2} \rangle$
18(3)	$0.6593 \pm \frac{5}{2} \rangle - 0.7518 \mp \frac{3}{2} \rangle$
0	$ \pm \frac{1}{2} \rangle$

($\alpha = x, y, z$) can be calculated as follows [12]:

$$\chi^{(\alpha)} = N_A (\mu_B g_j)^2 \left(\sum_{i=j} \frac{|\langle i | \hat{J}^{(\alpha)} | j \rangle|^2}{k_B T} n_i + \sum_{i \neq j} \frac{|\langle i | \hat{J}^{(\alpha)} | j \rangle|^2}{E_i - E_j} (n_j - n_i) \right) \quad (S6)$$

Here N_A is Avogadro's number and μ_B is the Bohr magneton. $|i\rangle$ is the eigenstate from the crystal field analysis corresponding to the eigenvalue E_i . \hat{J}^α are angular momentum operators associated with the three cartesian coordinates and n_i, n_j are the thermal population factors. The theoretical powder averaged susceptibility is calculated as $\chi = (2\chi^{(x)} + \chi^{(z)})/3$. The inverse susceptibility can then be fitted to $1/(\chi + \chi_0)$ where χ_0 is a temperature independent diamagnetic term. The corresponding fitting is shown as the red curve with CEF parameters listed in the caption of Fig. S8 without any additional parameters adjustable parameters except for $\chi_0 = -3.3e-3$ emu/Oe/mol. This consistency with susceptibility data further reinforces our conclusion that $| \pm \frac{1}{2} \rangle$ is the Kramers doublet ground state.

We can extract the inelastic spectral weight for each CEF mode E_n at low temperature $T = 7$ K as following:

$$\delta m_n^2 = 6\mu_B^2 \frac{\int \int Q^2 \tilde{I}_n(E) (1 + e^{-E\beta}) / |r_0 F(Q)|^2 dQ dE}{\int Q^2 dQ} \quad (S7)$$

$\tilde{I}_n(E)$ is momentum-integrated scattering defined in the main text. The sum of the observed inelastic spectral weight δm_n^2 and static moment $\langle m \rangle^2 (= 0.37^2 \mu_B^2)$ spin correlation yields a total spectral weight of $m_{tot}^2 = 6.0(4) \mu_B^2$ per Ce, consistent with the expected value $g_j^2 J(J+1) = 6.47 \mu_B^2$ with $g_j = \frac{6}{7}$. The magnitude of $\langle \mu_x \rangle =$

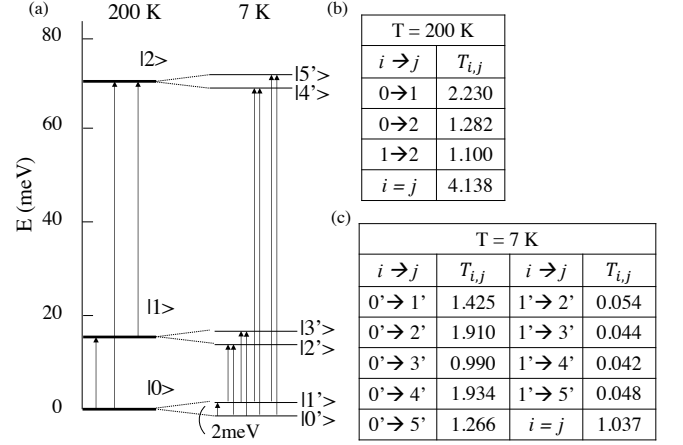


FIG. S7: (a) Graphic crystal field schemes for $T = 200$ K and 7 K. (b-c) The corresponding matrix elements $T_{i,j} = \sum_\alpha p_i |\langle i | J_\alpha | j \rangle|^2 (1 + e^{-E\beta})$ from the models. The sum over all matrix elements obeys the following sum-rule $\sum_{i,j} T_{i,j} = J(J+1)$

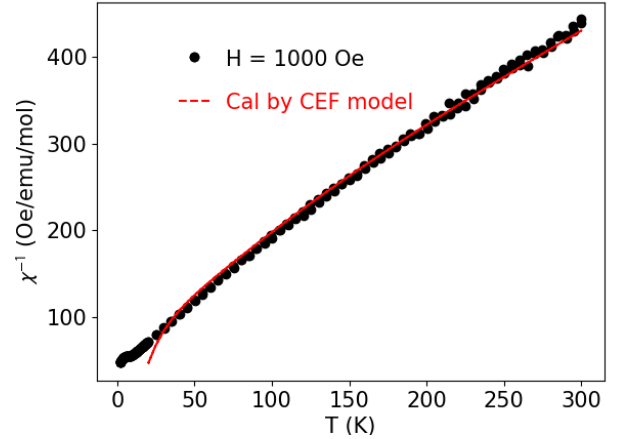


FIG. S8: Magnetic susceptibility of polycrystalline CeNiAsO as inferred from magnetization measurements in an applied field $H = 1000$ Oe. The red curve shows the calculated temperature dependent magnetic susceptibility based on the CEF model Eq. S6 and a small diamagnetic component that was adjusted for best agreement with the data. The corresponding coefficients of the Steven operators are $B_2^0 = 3.9(1.3)$, $B_4^0 = -0.05(3)$, $B_4^4 = 0.7(1)$.

$\langle \psi_0 | g_j J_x | \psi_0 \rangle$ with the ground state singlet listed in Table S4 is calculated as $0.9 \mu_B$, while the magnitude of $\langle \mu_z \rangle (= \langle \psi_0 | g_j J_z | \psi_0 \rangle) \sim 0$. This is consistent with the proposed in-plane spin structure.

- [1] T. McQueen, T. Klimczuk, A. Williams, Q. Huang, and R. Cava, Physical Review B **79**, 172502 (2009).
- [2] J. Rodriguez-Carvajal, in *Satellite meeting on powder diffraction of the XV congress of the IUCr* (Toulouse,

- France:[sn], 1990), vol. 127.
- [3] J. Zhao, Q. Huang, C. de La Cruz, S. Li, J. Lynn, Y. Chen, M. Green, G. Chen, G. Li, Z. Li, et al., *Nature Mat.* **7**, 953 (2008).
 - [4] G. Kresse and J. Furthmuller, *J. Comp. Materials* **6**, 15 (1996).
 - [5] G. Kresse, *Phys. Rev. B* **54**, 11169 (1996).
 - [6] G. Kresse and J. Hafner, *Phys. Rev. B* **43**, 558 (1993).
 - [7] C. Kittel, *Introduction to Solid State Physics* (Wiley, 2005).
 - [8] E. Heltemes and C. Swenson, *J. Chem. Phys.* **35**, 1264 (1961).
 - [9] C.D.Bredl, S.Horn, and F. Steglich, *Phys. Rev. Lett.* **52**, 22 (1984).
 - [10] K. W. H. Stevens, *Proc. Phys. Soc. A* **65**, 209 (1952).
 - [11] S. Lovesy, *Theory of magnetic neutron and photon scattering* (1989).
 - [12] J. Jensen, *J. Magn. Magn. Mater.* **29**, 47 (1982).